J. Fluid Mech. (2009), *vol.* 638, *pp.* 423–452.
doi:10.1017/S0022112009990772

On the structure of shear stress and turbulent kinetic energy flux across the roughness layer of a gravel-bed channel flow

EMMANUEL MIGNOT†, D. HURTHER
AND E. BARTHELEMY
Laboratoire des Ecoulements Géophysiques et Industriels (LEGI, UJF/INPG/CNRS),
BP 53, 38041 Grenoble, France

(Received 25 April 2008; revised 9 June 2009; accepted 10 June 2009; first published online 7 October 2009)

This study examines the structure of shear stress and turbulent kinetic energy (TKE) flux across the roughness layer of a uniform, fully rough gravel-bed channel flow ($k_s^+ \gg 100$, $\delta/k = 20$) using high-resolution acoustic Doppler velocity profiler measurements. The studied gravel-bed roughness layer exhibits a complex random multi-scale roughness structure in strong contrast with conceptualized k- or d-type roughness in standard rough-wall flows. Within the roughness layer, strong spatial variability of all time-averaged flow quantities are observed affecting up to 40 % of the boundary layer height. This variability is attributed to the presence of bed zones with emanating bed protuberances (or gravel clusters) acting as local flow obstacles and bed zones of more homogenous roughness of densely packed gravel elements. Considering the strong spatial mean flow variability across the roughness layer, a spatio-temporal averaging procedure, called double averaging (DA), has been applied to the analysed flow quantities. Three aspects have been addressed: (*a*) the DA shear stress and DA TKE flux in specific bed zones associated with three classes of velocity profiles as previously proposed in Mignot, Barthélemy & Hurther (*J. Fluid Mech.*, vol. 618, 2009, p. 279), (*b*) the global and per class DA conditional statistics of shear stress and associated TKE flux and (*c*) the contribution of large-scale coherent shear stress structures (LC3S) to the TKE flux across the roughness layer. The mean Reynolds and dispersive shear structure show good agreement between the protuberance bed zones associated with the S-shape/accelerated classes and recent results obtained in standard k-type rough-wall flows (Djenidi *et al.*, *Exp. Fluids*, vol. 44, 2008, p. 37; Pokrajac, McEwan & Nikora, *Exp. Fluids*, vol. 45, 2008, p. 73). These gravel-bed protuberances act as local flow obstacles inducing a strong turbulent activity in their wake regions. The conditional statistics show that the Reynolds stress contribution is fairly well distributed between sweep and ejection events, with threshold values ranging from $H = 0$ to $H = 8$. However, the TKE flux across the roughness layer primarily results from the residual shear stress between ejection and sweep of very high magnitude ($H = 10$–20) and of small turbulent scale. Although LC3S are seen to penetrated the interfacial roughness layer, their TKE flux contribution is found to be negligible compared to the very energetic small-scale sweep events. These sweeps are dominantly produced in the bed zones of local gravel protuberances where the velocity profiles are inflexional of S-shape type and the mean flow properties are of mixing-layer flow type as previously shown in Mignot *et al.* (2009).

---

† Email address for correspondence: emmanuel.mignot@hmg.inpg.fr

1. Introduction

The benthic boundary layer in gravel-bed river flows has received much attention in the past years because macro-roughness strongly influences ecological processes in the river environment at all scales. Examples are transport, fate and mixing of an extreme diversity of river substances such as dissolved or particulate nutrients and contaminants, natural sediments and benthic living organisms. New insights into the hydrodynamic mechanisms and properties above and across the flow/gravel-bed interface are necessary to improve our understanding of these coupled flow processes.

The literature results on rough-wall flows primarily focused on two-dimensional and three-dimensional artificial roughness presenting a highly organized and periodic wall roughness structure. The ranges of dimensionless parameters k_s^+ (roughness Reynolds number based on the equivalent sand roughness k_s and the bed friction velocity u_*), k/δ (ratio between roughness size k and boundary layer thickness δ) and λ (the solidity, defined as the total projected frontal roughness area per unit wall-parallel projected area by Schlichting 1936) allow to distinguish between two main categories of roughness with their corresponding underlying flow mechanisms (Perry, Schofield & Joubert 1969; Jimenez 2004; Castro 2007). The first is the so-called k-type roughness for which the streamwise distance between the roughness elements is sufficient (typically greater than $8k$) to consider obstacles inducing flow detachment and reattachment in the turbulent wake regions downstream each roughness element (Djenidi *et al.* 2008). The form drag acting on the flow can then be related to the frontal exposure area of the roughness elements and it induces turbulent momentum exchange between the roughness layer and the inertial layer via the stress terms (mainly Reynolds shear stress and dispersive stress, see Pokrajac, McEwan & Nikora 2008). Two regimes are encountered for such k-type roughness. For low values of solidity λ up to a critical value of about 10 %, the equivalent sand roughness k_s increases with λ for a wide variety of roughness elements. Above the critical solidity value, the transition regime to d-type roughness begins and k_s decreases with solidity. In this transition regime, the distance between neighbouring elements becomes smaller than the flow reattachment distance and sheltering/wake interferences occur. The second roughness category is the so-called d-type roughness for which the distance between roughness elements is typically smaller than $3k$. The d-type is characterized by a correlation of k_s with the boundary layer thickness itself instead of the geometrical characteristics of the roughness elements. This outer flow scaling is associated with a flow skimming behaviour sustaining a quasi-steady flow circulation within the 'small' roughness cavities as shown by flow observations in Liou, Chang & Hwang (1990) and Djenidi *et al.* (1994). This is believed to strongly reduce the form drag forcing of the vertical momentum exchange across the roughness layer compared to the case of k-type roughness.

The majority of gravel-bed open-channel or river flows enter in the category of fully rough shear flows ($ks^+ \gg 70$) with flow submergences in the range of $k/\delta < 0.1$. However, the high degree of spatial heterogeneity associated with the absence of periodicity in bed elevation is in strong contrast with idealized k- or d-type rough-wall roughness structure. As shown in figure 1, the gravel-bed elevation irregularities occur at the scale of the mean gravel size (equal to 2 cm in our case) over roughly 70 % of the measurement section ($4 < x < 4.15$ and $4.38 < x < 4.9$) while the remaining bed region is composed of local bed protuberances (noted P) which are clusters of several gravel elements (at $x = 4.2$ and $x = 4.31$ in figure 1). This complex multi-layer roughness structure supports stronger similarities with the roughness structure of urban canopies rather than with idealized organized wall roughness. Urban canopies

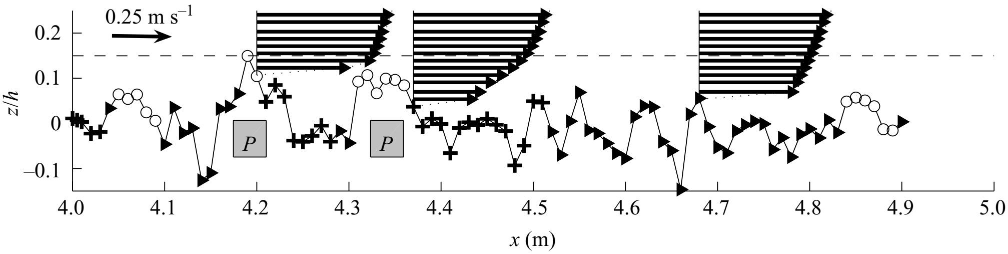

FIGURE 1. Local mean streamwise velocity from acoustic Doppler velocity profiler (ADVP) measurements along with bed topography (-) measured by the digital point gauge, crest level (- -) and protuberances (*P*). Profiles are associated with a symbol, drawn at the bottom, representing the class to which they pertain: (►): log; (+) S-shape; (○): accelerated.

of big cities can be constituted of many irregularly shaped low-level buildings in the lower part of the interfacial sublayer with few emergent high buildings in its upper part (Roth 2000; Cheng & Castro 2002; Coceal *et al.* 2006). As a consequence, the vertical dimension of the roughness layer is strongly increased and the lower limit of the inertial layer lies much higher than for rough-wall flows over idealized k- and d-type roughness.

This behaviour has also been observed in gravel-bed channel and river flows for which the heterogeneous gravel-bed roughness structure is associated with a high spatial variability of the local time-averaged velocity profiles across the roughness layer (Nikora *et al.* 2001; Franca 2005). The three time-averaged velocity profiles represented in figure 1 denote this spatial variability for the gravel-bed flow studied herein. These strong mean flow non-uniformities (although the flow is uniform in average at scales much higher than the gravel scale) motivated the application of double averaging (DA) methods in open-channel hydrodynamics (Lopez & Garcia 2001; Nikora *et al.* 2001). Originally, this technique had been applied to atmospheric canopy wind flows for the same reason (Raupach, Antonia & Rajagopalan 1981, 1991; Finnigan 2000).

Mignot, Barthélemy & Hurther (2009) derived and discussed the DA momentum and turbulent kinetic energy (TKE) budgets for the gravel channel flow studied herein. It could be shown that the DA shear stress reaches its maximum value at the top of the interfacial sublayer noted z_c (bed crest level represented by the dashed line in figure 1) with a very limited contribution of the DA dispersive stress (see figures 5*a* and 5*b*). Furthermore, the maximum shear production in the DA TKE budget occurs slightly below the top of the interfacial sublayer. The DA TKE flux is seen to be oriented towards the free surface above the upper limit of the interfacial sublayer ($z > zc$), and towards the bed beneath it. These results reveal that the turbulent energy produced at elevations near z_c is transported away in both vertical directions. Furthermore, the analysis of the local time-averaged flow velocity profiles along the stretch of bed topography plotted in figure 1 shows that the classification of the local streamwise velocity profiles as proposed by Hoover & Ackerman (2004) is also persistent in our gravel-bed flows. Three classes are observed and we show in figure 1 that this classification is dependent on the positions of the profiles relative to the local bed protuberances P. The log-class corresponds to profiles located outside the flow regions affected by local bed protuberances (see bed locations with ‘triangle’ signs in figure 1). The accelerated-class profiles are located near the top of the bed protuberances (‘circle’ signs in figure 1) and the S-shape-class profiles are located in the wakes downstream of the protuberances ('plus' signs in figure 1). The log-class profiles exhibit similar TKE production, diffusion and dissipation profiles as the corresponding DA terms whereas the corresponding terms for the S-shape class exhibit strong similarities with detached mixing layers. It is found that the S-shape zone only represents 25 % of all classes at the bed but is responsible for 50 % of the total DA shear production in the roughness layer of gravel-bed flows.

In order to examine the detailed structure of shear stress and TKE flux in a gravel-bed flow, this study will first present the DA shear stresses (Reynolds stress and dispersive stress), the DA correlation coefficients and the DA TKE flux profiles across the gravel-bed roughness layer for the three specific classes (or bed zones). A comparison with the DA shear stress and correlation coefficient profiles recently measured by Pokrajac *et al.* (2008) and Djenidi *et al.* (2008) in organized k- and d-type rough-wall flows will be done. Whether the specific classes (i.e. bed zones) of our gravel-bed flow show similarities with a given type of standard rough-wall flow will be addressed. The second part of this study is devoted to the global DA and per class DA characteristics of conditionally sampled Reynolds shear stress and associated TKE flux. For this purpose, we will apply a quadrant threshold method to Reynolds stress and TKE flux events and compare the results to literature data obtained in standard rough-wall flows (Nakagawa & Nezu 1977; Raupach *et al.* 1981; Hurther, Lemmin & Terray 2007) and a corn field canopy flow (Yue *et al.* 2007). Whether the quadrant dynamics is locally affected by the presence of bed protuberances will be addressed here.

The last part of the study is devoted to the coherent shear stress events represented by the thick contour lines in figure 2 for the three bed zones. These structures are closed contours of turbulent velocity vectors belonging to a given quadrant and with a given threshold level (fixed to $H=2$). Such large-scale coherent flow structures were previously reported by authors such as Sumer & Deiggard (1981) in the form of quasi-cyclic events scaling with the outer flow parameters and Grass, Stuart & Mansour-Tehrani (1991) as vertical structures scaling with the size of the boundary layer. More recently, Hurther *et al.* (2007) defined such coherent structures as large coherent shear stress structures (LC3S) associated with the organization into macro-scale packets of detached hairpin vortices in the outer flow region. Their contribution to the mean vertical TKE flux was seen to be dominant across the outer flow region of a rough-wall channel flow (Hurther *et al.* 2007). Surprisingly, figure 2 reveals that LC3S in the herein studied gravel-bed flow do penetrate the gravel-bed roughness layer in all three types of bed zone (for example, at $tU/h=2$ and $tU/h=3.5$ in figure 2*a*). How LC3S affect the roughness layer hydrodynamics is the third objective of this study. For this purpose, the LC3S contributions to DA shear stress and TKE flux will be evaluated and discussed.

2. Experimental set-up and flow conditions

The experiments are conducted at the LEGI (Grenoble, France), in a 35 cm wide and 9 m long rectangular flume with a slope S_0 of 0.2 %. A stationary uniform subcritical flow is obtained at the centre of the flume where measurements are performed. Global hydraulic parameters of the flow are given in table 1. The bed is composed of about two layers of angular-crested gravel elements (stones) of $d_{50}=2$ cm which were deposited randomly on the bottom of the channel without any specific arrangement see figure 3). The irregular arrangement of the sediment on the bottom results in localized macro-roughness elements (protuberances composed of a few stones) such as

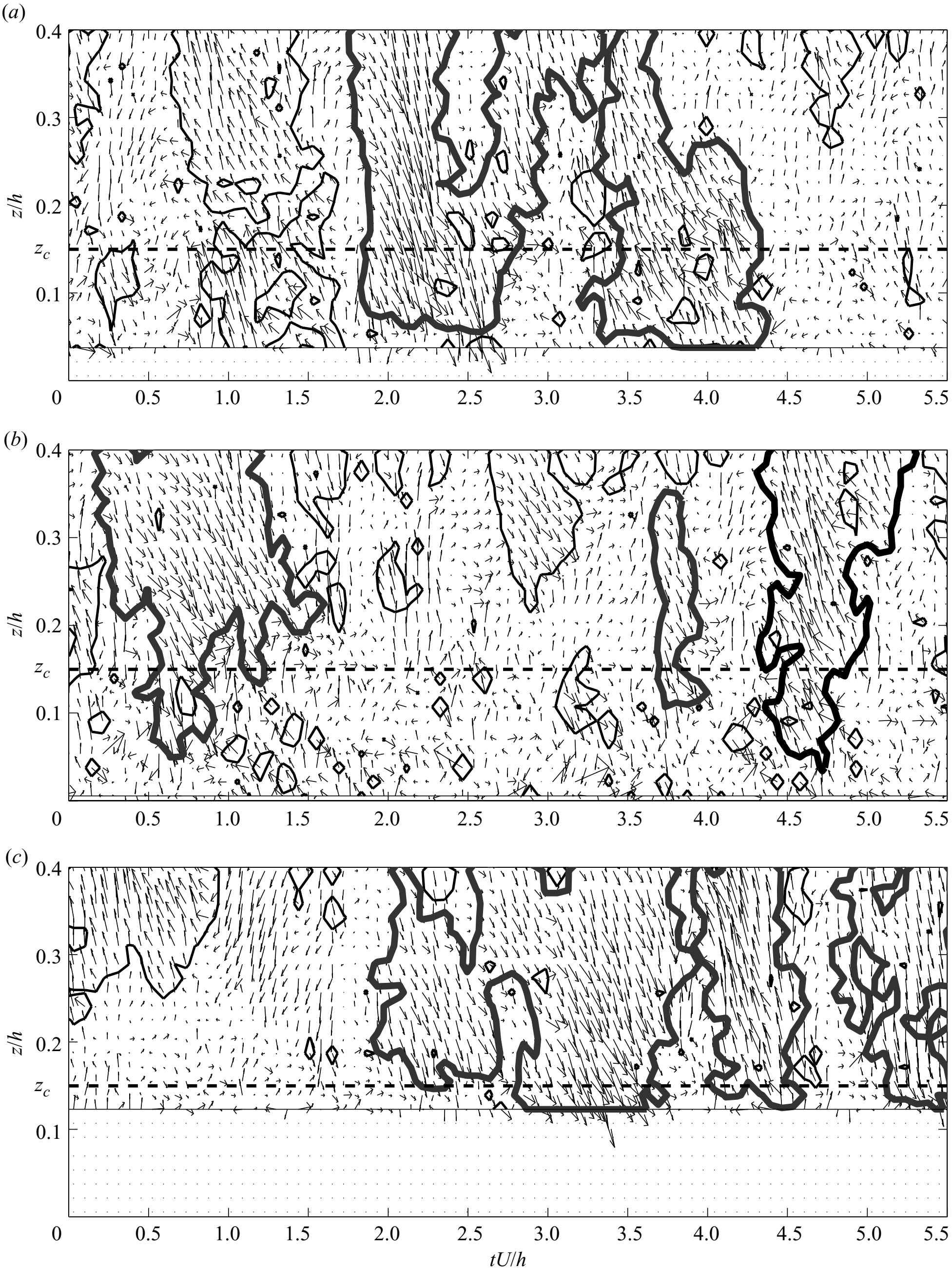

FIGURE 2. Time series of local instantaneous velocity fields (arrows) and coherent Reynolds stress structures with $H = 2$ (plain lines) at a: $x = 4.7$ m (log-class), b: $x = 4.4$ m (S-shape-class) and c: $x = 4.2$ m (accelerated-class), where thicker lines are LC3S (Horizontal dash line is z_c elevation and horizontal plain line is local bed elevation). The 'x-axis' label is time normalized by bulk velocity U and water depth h.

at $x \backsim 4.2$ m and $x \backsim 4.31$ m in figure 1. The studied area is located between $x = 4$ m and 4.9 m downstream from the channel entrance. The bed topography is surveyed along the centreline of the channel using a digital point gauge. The reference plane

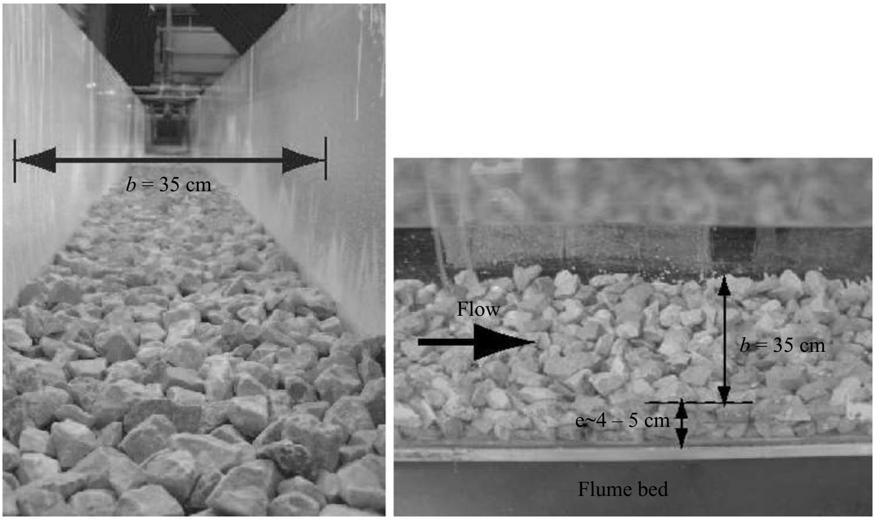

FIGURE 3. Upstream and side views of the flume and gravel-bed with b the channel width and e the gravel-bed thickness.

S_0 (%)	Q (l s^{-1})	$h=\delta$ (mm)	U (m s^{-1})	$Re=$ Uh/ν	Fr	u_* (m s^{-1})	$Re_*=$ u_*h/ν	k_s (mm)	$k_s^+=$ u_*k_s/ν	z_c (mm)	λ_T (mm)	η (mm)
0.2	40.4	187	0.62	115 400	0.46	0.053	9911	11	583	28	4.7	0.11

TABLE 1. Hydraulic parameters: S_0 the channel slope, Q the discharge, h the water depth (measured as the distance between the sediment crests at z_c and the water surface) and δ the boundary layer height, U the bulk velocity, Re the Reynolds number, Fr the Froude number, u_* the friction velocity, $Re*$ the friction Reynolds number, k_s the Nikuradse equivalent roughness size obtained by the Clauser-type fitting of the double-averaged velocity profile, k_s^+ the roughness Reynolds number, z_c the sediment crest level, $\lambda_T = (15\nu < \overline{u'^2} > / < \epsilon >)^{1/2}$ the DA Taylor scale computed at $z = z_c$, $\eta = (\nu^3 / < \epsilon >)^{1/4}$ the DA Kolmogorov scale computed at $z = z_c$ where ϵ is computed using a standard turbulent macro-scale formulation (see Mignot *et al.* 2009).

$z = 0$ is defined as the average measured bed elevation. We define the roughness layer as the benthic flow region (below the inertial layer) affected by the bed roughness. In this region, the local time-averaged flow quantities vary spatially due to roughness effects as seen in figure 1 for the mean velocity profiles. The upper limit of the roughness layer where most class-averaged flow quantity profiles converge to a single curve is equal to 0.38 h in our case (see figure 5), with h the water depth. The interfacial sublayer represents the lower part of the roughness layer with its upper limit corresponding to the bed crest level z_c (highest bed elevation above the reference plane across the measurement section) as defined by Nikora *et al.* (2001). For our bed topography, z_c is located 2.8 cm above the reference plane at $z_c/h = 0.15$.

The flow measurements are performed using a high-resolution 4-receiver acoustic Doppler velocity profiler (ADVP) located at the centreline of the channel. This measuring tool provides the velocity components along the three orthogonal coordinates at high rate (typically 50–100 Hz) along a vertical line of about 15 cm with a 3 mm vertical step resolution. As seen in figure 2, the profiling ability of the device is of particular interest for the combination of conditional flow statistics and the visualization of the conditionally sampled flow patterns across the boundary layer. Consequently, ADVPs have been used extensively in the past 10 years for detailed turbulence studies in open-channel flows (Song, Graf & Lemmin 1994; Hurther & Lemmin 2000, 2003; Blanckaert & de Vriend 2004, 2005; Hurther *et al.* 2007). A detailed description of the ADVP principles, performances and limits can be found in Lemmin & Rolland (1997), Hurther & Lemmin (2001), Blanckaert & de Vriend (2005) and Hurther & Lemmin (2008). In the present experiment, the collected profiles extend over the lower half of the water column, with u, v, w, the streamwise, transverse and vertical measured velocity components, respectively, along the x-, y- and z-axis. The measurement volumes can be approximated as vertical cylinders of 3 mm height and maximal diameter of about 2 cm (−6dB acoustic intensity at 20 cm away from the emitter). It has been shown in Hurther & Lemmin (2001) and Hurther & Lemmin (2008) that accurate estimations of turbulent micro-scales are obtained for flow scales in the centimetre range.

Each profile presented in the paper is obtained from a 300 s time length sampled at a frequency of 46.9 Hz (the pulse repetition frequency was set to 1500 Hz and the quasi-instantaneous velocity estimations were averaged over 32 consecutive echoes for an optimal resolution/accuracy setting). Vertical velocity profiles are measured at 45 locations along the channel centreline within the 90 cm long measurement section (see figure 1). The streamwise spacing of the verticals is fixed to 2 cm. For more details on the experimental installation, measuring device and measurement methodology, we refer the reader to the paper of Mignot *et al.* (2009).

Due to the small width-to-depth ratio of our open-channel flow, two symmetric secondary cells were observed with respect to the flume centre-plane. However, several precautions were taken to minimize secondary flow dependence of our results. First, the bed is very rough while the sidewalls are smooth. The aspect ratio is then less severe in our flow configuration than in the case where the bottom and sidewalls would be equally rough. Moreover, the streamwise flow uniformity was checked out over a streamwise distance of 2 m. This avoids any streamwise variation of the flow statistics due to secondary cells. Therefore, the discussed spatial variability of the flow quantities across the roughness layer can only be attributed to gravel-roughness effects especially at the scale of the roughness element size. Furthermore, as presented above, the DA quantities are actually lineic averages along the centreline of the channel where the secondary cells are uniform in mean. Consequently, the spatial variations of all the discussed flow variables in x direction cannot be strongly affected by these secondary cells. Also, the study focuses on flow processes across the roughness sublayer with a vertical height scaling with the mean gravel size, i.e. one order of magnitude smaller than the size of a secondary cell. As a consequence, the discussed flow characteristics are attributed to macro-roughness effects across the roughness sublayer.

As described in Mignot *et al.* (2009), the friction velocity u_*, the displacement height Δz and the equivalent Nikuradse roughness size k_s were obtained from a Clauser-type analysis on the double-averaged streamwise velocity profile (see table 1). The displacement height Δz was found to be very small $\Delta z \approx -0.15k_s$, the Nikuradse zero-plane displacement is therefore located at the mean bed elevation. However, the choice of the upper elevation limit in the Clauser-type fitting process can strongly affect the value of these parameters (see table 2). The values in table 1 give the highest correlation factor between the log fit and the measured data, corresponding to an upper limit $(z/h)_{lim}$ slightly lower than 0.3.

	$(z/h)_{lim}=0.3$	$(z/h)_{lim}=0.2$	$(z/h)_{lim}=0.1$
u_* (m s^{-1})	0.053	0.065	0.044
k_s (mm)	17	43	6.5
Δz (mm)	−7.4	0	−11

TABLE 2. Influence of the top limit $(z/h)_{lim}$ on the Clauser-fitting process results.

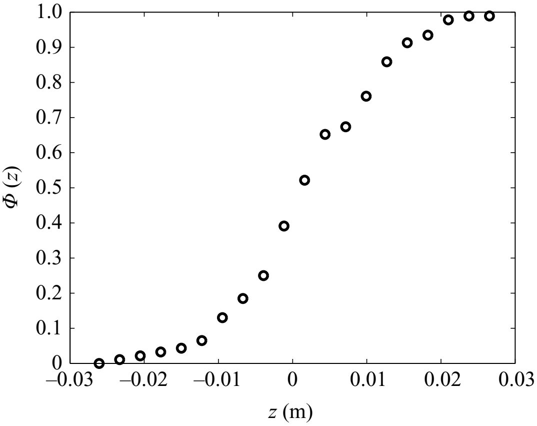

FIGURE 4. Gravel-bed roughness function measured by the digital point gauge.

3. Mean structure of double averaged shear stress and TKE flux

The DA methodology applied herein is identical to the one used in Nikora *et al.* (2007) and Mignot, Barthélemy & Hurther (2008) for the Momentum and TKE budget variables. For a slowly varying flow, the DA variables are calculated as

$$\langle\overline{\theta}(\boldsymbol{x})\rangle = \frac{1}{A_0}\int_{A_f}\overline{\theta}(\boldsymbol{x}+\boldsymbol{r})\,\mathrm{d}S \tag{3.1}$$

for any local time-averaged variable $\overline{\theta}$, where <> denotes the spatial averaging, A_f is the area occupied by the fluid at a given elevation z within the total averaging area A_0 at this given elevation. Here, $\boldsymbol{r}$ is the vector describing A_f around location point $\boldsymbol{x}$, and dS is an infinitesimal area element. The so called superficial DA methodology (defined in (3.1)) is used here because both Reynolds shear stress and TKE flux terms appear as superficial averages in the DA momentum and TKE budgets respectively (see Nikora *et al.* 2007; Mignot *et al.* 2008). The interfacial roughness function can then be expressed as $\Phi(z)=A_f/A_0(z)$. It represents the statistical distribution of bed elevation measured over the whole studied area (see figure 1) using the digital point gauge. It is a z-dependent function equal to unity above the bed crest level z_c (i.e. outside the interfacial sublayer). Below z_c, it decreases towards 0. The roughness function for the studied gravel bed is shown in figure 4. The region delimited by the roughness function varying between zero and unity defines the gravel-bed interfacial sublayer (Nikora, Goring, McEwan & Griffiths 2001; Aberle 2007; Mignot *et al.* 2009). It is noteworthy that the complement of the roughness function corresponds to an approximation of the solidity distribution across the interfacial sublayer.

As previously shown (Pokrajac *et al.* 2008; Mignot *et al.* 2009), the normalized total shear stress appearing in the DA momentum equation can be decomposed into the sum of the DA Reynolds shear stress and the DA dispersive shear stress (the viscous stress term being neglected):

$$\frac{\tau_{xz}}{\rho u_*^2} = -\frac{\langle\overline{u'w'}\rangle}{u_*^2} - \frac{\langle\tilde{u}\tilde{w}\rangle}{u_*^2}, \tag{3.2}$$

where the local instantaneous velocity components are decomposed into $u_j = \overline{u_j} + u'_j$ and the local time-averaged velocity components into $\overline{u_j} = \langle\overline{u_j}\rangle + \tilde{u}_j$. The angular brackets, overbar, prime and tilda signs denote the spatially-averaged, time-averaged, time-fluctuation and spatial-fluctuation, respectively. When applying this decomposition and averaging (first in time and then in space) to the TKE budget equation, the normalized DA vertical TKE flux can be written as (see Mignot *et al.* 2009)

$$\frac{F}{u_*^3} = \frac{\langle\overline{k'w'}\rangle}{u_*^3} + \frac{\langle\tilde{k}\tilde{w}\rangle}{u_*^3}, \tag{3.3}$$

with $k' = 1/2(u'^2 + v'^2 + w'^2)$. The first and second terms on the right-hand side of (3.3) are the DA vertical main TKE flux and DA vertical dispersive TKE flux, respectively.

In contrast with previous works, these terms are examined here for each class meaning that the spatial averaging in the double averaging procedure is applied to the specific gravel-bed zone associated with each individual class of mean velocity profile (Mignot *et al.* 2009).

Figures 5(*a*) and 5(*b*) show the resulting profiles for the normalized DA Reynolds and dispersive shear stresses normalized by the squared bed friction velocity, respectively. As previously shown in Mignot *et al.* (2009), the DA Reynolds shear stress for the S-shape-class shows significant higher values than the values measured in the log and accelerated classes within the interfacial sublayer. The dispersive shear stress for the log-class remains low across the roughness layer whereas it reaches a positive maximum and minimum value of 0.13 and −0.05 respectively, in the interfacial sublayer for the S-shape class. Above the interfacial sublayer, only the dispersive stress associated with the accelerated-class has a non negligible negative value vanishing at the top of the roughness layer. When compared to the DA dispersive shear stress profiles measured separately for k- and d-type roughness by Pokrajac *et al.* (2008), the S-shape-class profile shows a better agreement with the d–k transition case than with the d- or k-type cases. In particular, a maximum positive DA dispersive shear stress value of 0.12 is measured by Pokrajac *et al.* (2008) close to the top of the interfacial sublayer being very close to the value of 0.13 found for the S-shape class (see figure 5*b*). Finally, in figure 5(*b*), the log-class shows smaller absolute dispersive stress values supporting the fact that form drag might be smaller in densely packed roughness zones closer to d-type roughness than in sparse packed zones of k-type roughness such as the protuberance bed zones.

Figures 5(*c*) and 5(*d*) represent the profiles of the correlation coefficients for the Reynolds (r_R) and dispersive stress (r_D), defined as

$$r_R = \frac{-\langle\overline{u'w'}\rangle}{(\langle u'^2\rangle\langle w'^2\rangle)^{1/2}} \tag{3.4}$$

and

$$r_D = \frac{-\langle\tilde{u}\tilde{w}\rangle}{(\langle\tilde{u}^2\rangle\langle\tilde{w}^2\rangle)^{1/2}}. \tag{3.5}$$

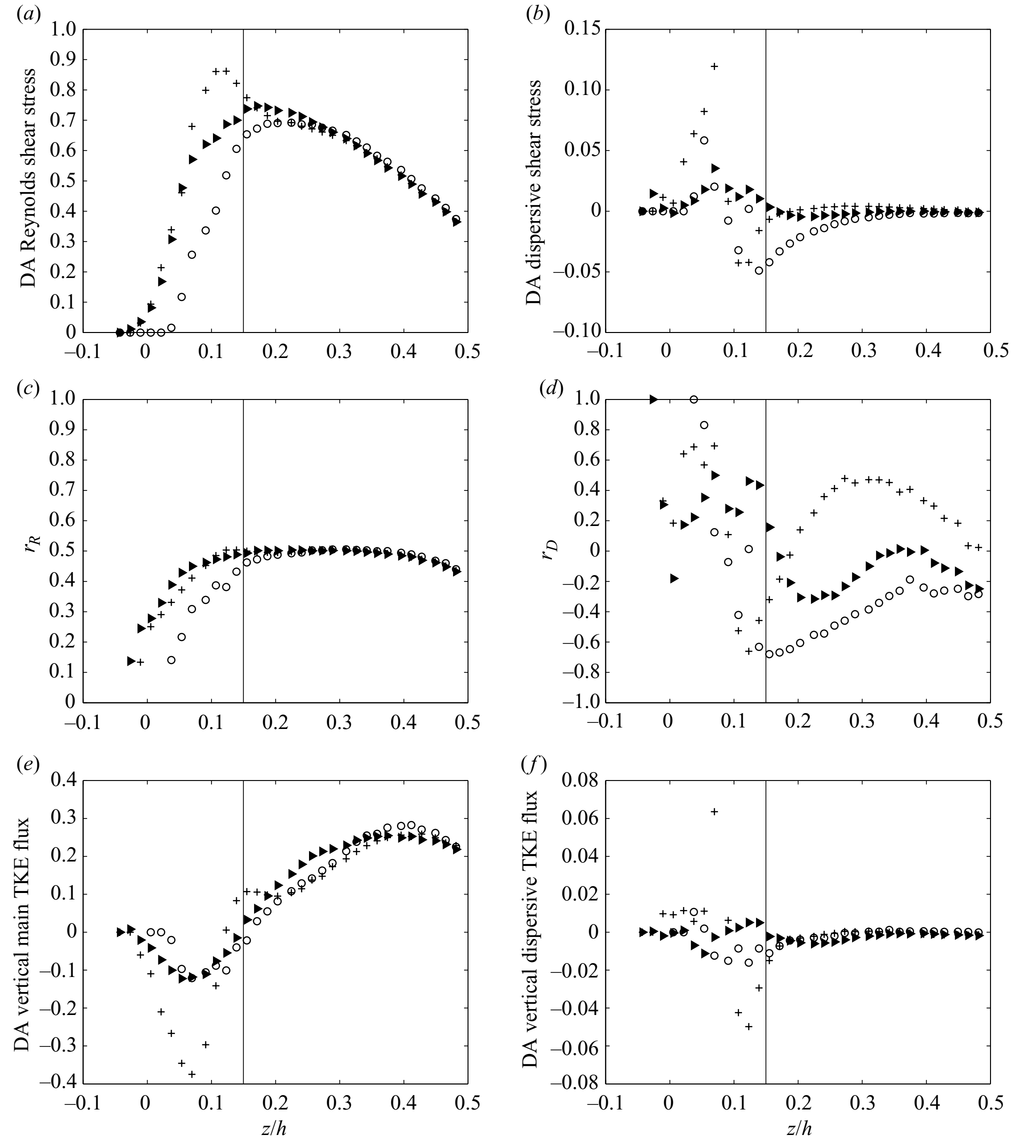

FIGURE 5. Vertical profiles of per class averaged Reynolds (*a*) and dispersive (*b*) shear stress normalized by the squared DA friction velocity; double averaged correlation coefficients for the Reynolds (*c*) and dispersive (*d*) shear stress; double averaged vertical main (*e*) and dispersive (*f*) TKE flux normalized by the cubic DA friction velocity. (+): S-shape, (○): accelerated and (▶): log class. Vertical plain line refers to z_c elevation. The scales of vertical axis in (*a*)–(*e*) (main quantities) and (*b*)–(*f*) (dispersive quantities) are unequal.

It is seen in figure 5(*c*) that the Reynolds correlation coefficients r_R above the interfacial sublayer have a similar value of 0.5 in the three bed zones. This value is in good agreement with previous results found in the inertial sublayer of standard rough-wall shear flows (Nezu & Nakagawa 1993). Within the interfacial sublayer, the accelerated and S-shape classes show lower correlation values with proximity to the bed than those obtained for the log-class. This might be explained by the difference in roughness structure between the bed zones associated with the log-class and the

S-shape/accelerated classes. Djenidi *et al.* (2008) showed recently for two separate cases of k-roughness type that the DA Reynolds correlation decreases in the roughness layer with the increase of the separation distance between roughness elements (noting that their k/h range is very similar to the one herein). In our S-shape and accelerated classes, the separation distance is seen to be much larger than in the log-class as the protuberance bed zones associated with the S-shape and accelerated classes rather correspond to obstacle regions with separation distances of about $5k$–$8k$ (see figure 1 with $k \cong d50/2 \cong 1$ cm). The lower correlation in the accelerated and S-shape classes in figure 5(c) is then in agreement with Djenidi *et al.* (2008) measurements. Djenidi *et al.* (2008) also observed that the vertical region over which the correlations have different values extended over a length of about $15k$ (0.35δ) starting from the bed. In our case, this region only extends over a distance of about $4k$, correponding to $0.21h$. This confirms Djenidi *et al.*'s statement that k-type roughness can affect the flow well beyond the near-wall region at moderate flow submergences (Djenidi *et al.* 2008).

Figure 5(d) shows the profiles of dispersive correlation coefficients. Compared to the Reynolds stress correlations, more pronounced differences are seen between the classes all across and above the roughness layer. Moreover, as for the dispersive stress in figure 5(b), the log-class shows smaller absolute values of correlation than the S-shape class.

Figure 5(e) shows the profiles of normalized DA main TKE flux measured in each of the three bed zones. It is seen that all three fluxes are positive above the interfacial sublayer and negative (oriented downwards) within this sublayer with a much more important negative flux for the S-shape class. As previously discussed in Mignot *et al.* (2009), it is seen that turbulent energy produced at a maximal rate at the top of the interfacial sublayer (not shown here) is transported by turbulent diffusion in both directions. Figure 5(f) reveals that within the interfacial sublayer, TKE linked to the dispersive terms can be diffused vertically in both directions with a dominant contribution in the S-shape bed zone. The differences in trends between the three classes are more pronounced than for the DA main TKE flux; however, the magnitudes of the fluxes are at least five times lower.

4. Double averaged conditional statistics: principles and method

Since the late seventies, the study of conditional statistics of shear stress has provided insights into the dynamics of momentum and TKE transfer in wall bounded water or atmospheric flows (Antonia & Atkinson 1973; Lu & Willmarth 1973; Nakagawa & Nezu 1977; Raupach *et al.* 1981; Luchik & Tiederman 1987; Robinson 1991; Pokrajac *et al.* 2007; Yue *et al.* 2007). The most used conditional sampling technique is known as the quadrant threshold technique originally applied to local measurements or simulations of the Reynolds shear stress term. When combined to flow visualization capabilities of the conditionally sampled flow events such as shown in figure 2 (and § 7), this statistical tool provides further information on the spatio-temporal scales of the most energetic turbulent eddies. More recently this statistical method has further been applied to heat flux in atmospheric boundary layers (Christen, Van Gorsel & Vogt 2007) and to sediment fluxes in open-channel flows (Hurther & Lemmin 2003) in order to identify the role played by turbulent flow structures in heat and sediment transport. In Hurther *et al.* (2007), the quadrant method has been applied to TKE flux events associated with conditionally sampled shear stress events in order to determine the flow structures responsible for the TKE transport across the outer region of a standard rough-bed open-channel flow.

Due to the strong spatial variability of the local mean flow quantities across the gravel-bed roughness layer, we are interested here in the DA conditional statistics of Reynolds shear stress and associated vertical TKE flux. In § 5, the spatial averaging in the DA process will be applied over the entire measuring section (global DA variables). In § 6, the DA quadrant threshold variables in the specific bed zones associated with the three classes will be calculated and discussed (bed zone specific DA variables).

The following local quadrant threshold variables will be calculated and analysed in the sequel:

$$RS_q(z, H) = T^{-1} \int_0^T \gamma(z, t) D(\gamma)\, \mathrm{d}t, \tag{4.1}$$

$$RS_q^*(z, H) = \frac{\langle \overline{u'w'(z)} \rangle}{u_*^2} RS_q(z, H), \tag{4.2}$$

$$T_q(z, H) = T^{-1} \int_0^T D(\gamma)\, \mathrm{d}t, \tag{4.3}$$

$$Fk_q(z, H) = T^{-1} \int_0^T \alpha(z, t) D(\gamma)\, \mathrm{d}t, \tag{4.4}$$

$$\left.\begin{aligned} Fk_q^-(z, H) &= T^{-1} \int_0^T \alpha(z, t) D^-(\gamma)\, \mathrm{d}t, \\ &= Fk_q(z, 0) - Fk_q(z, H) \end{aligned}\right\} \tag{4.5}$$

with the following notations

$$\gamma(z, t) = \frac{u'w'(z, t)}{\langle \overline{u'w'(z)} \rangle},$$

$$\alpha = \frac{1}{2u_*^3}(u'^2 w' + v'^2 w' + w'^3),$$

$$D(\gamma) = \begin{cases} 1 & \text{for } |\gamma| \geqslant H \text{ and } \gamma \text{ in } q \\ 0 & \text{otherwise} \end{cases},$$

$$D^-(\gamma) = \begin{cases} 1 & \text{for } |\gamma| \leqslant H \text{ and } \gamma \text{ in } q \\ 0 & \text{otherwise} \end{cases},$$

where T is the signal duration (300 s in the present case), H the so-called 'Threshold level', $u'w'(z, t)$ is the instantaneous velocity correlation involved in the local Reynolds stress $-\rho u'w'(z, t)$ and $-\rho \overline{u'w'}(z)$ is the time-averaged local Reynolds stress.

The four quadrants are referred to as: 'outward' (q = I with $u' > 0$ and $w' > 0$), 'ejections' (q = II with $u' < 0$ and $w' > 0$), 'inward' (q = III with $u' < 0$ and $w' < 0$) and 'sweeps' (q = IV with $u' > 0$ and $w' < 0$). The standard RS_q term gives the Reynolds stress value for the given quadrant q and threshold level H, relative to the DA Reynolds shear stress. RS_q^* is the Reynolds stress value normalized by u_*^2. $T_q(z, H)$ is the time fraction related to quadrant q for events stronger than H. The TKE flux

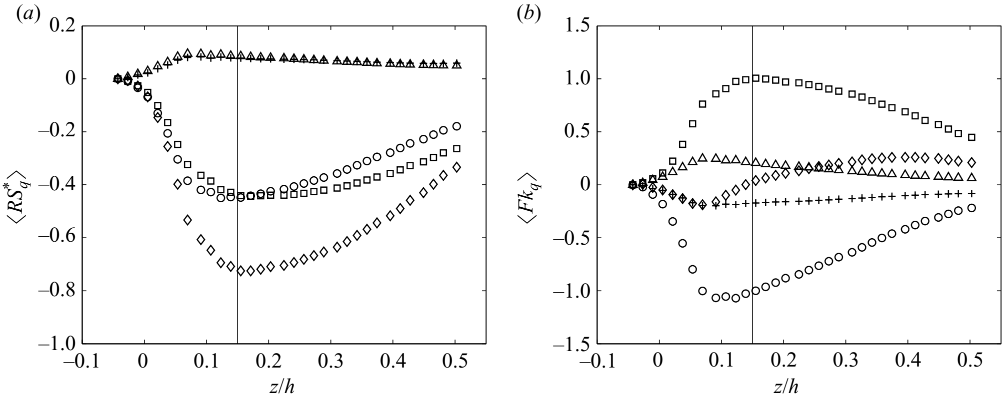

FIGURE 6. Double averaged normalized Reynolds stress (*a*) and TKE flux (*b*) contribution from the four quadrants ($H = 0$) with (◇): total, (△): $q =$ I, (□): $q =$ II, (+): $q =$ III, (○): $q =$ IV.

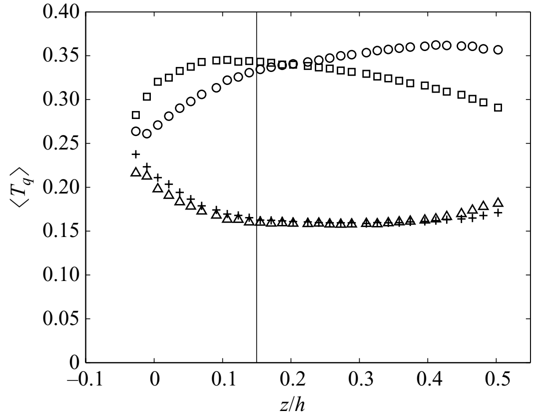

FIGURE 7. Duration fraction for the four quadrants ($H = 0$). See figure 6 for legend.

term $Fk_q(z, H)$ is the flux associated with Reynolds stress events in quadrant q for events stronger than H while $Fk_q^-(z, H)$ is the flux term for events weaker than H.

5. Global DA quadrant threshold results

5.1. *Quadrant specific signatures of DA variables*

In this first step, we compare the quadrant specific contributions considering the entire Reynolds stress time series, i.e. for a threshold level $H = 0$. Figure 6 presents the DA Reynolds stress $\langle RS_q^* \rangle$ (defined in (4.2)) and $\langle Fk_q \rangle$ (defined in (4.4)) contribution from the four quadrants. The total contribution (sum of the four quadrants) is also shown for both quantities. Figure 7 shows the time fraction $\langle T_q \rangle$ (defined in (4.3)) from all quadrants.

5.1.1. *Reynolds stress contribution*

It appears in figure 6(*a*) that quadrants I and III (quadrants with positive velocity correlation $\overline{u'w'}$, thus negative Reynolds stress contribution) have a very limited contribution to the total Reynolds stress profiles. Most of the stress contribution is related to quadrants II (ejections) and IV (sweeps), with negative velocity correlation (positive Reynolds stress values) corresponding to shear stresses. Both ejection and sweep contributions have similar values and general trends over the entire profile. The profiles increase towards the bed and reach their maximum values at the bed crest level z_c. Within the interfacial sublayer, the rapid decrease of the roughness function (figure 4) forces all contributions to 0.

The ejection contribution exceeds the sweep contribution above the interfacial sublayer whereas the opposite occurs within the interfacial sublayer. The overall characteristics of the DA quadrant distributions are in good agreement with those measured and simulated in standard uniform rough-wall flows (Grass 1971; Raupach *et al.* 1981; Hurther & Lemmin 2000) and in canopy flows (Finnigan 2000; Yue *et al.* 2007).

5.1.2. *TKE flux contribution*

As for the Reynolds stress contribution, figure 6(*b*) reveals that quadrants I and III have limited $\langle Fk \rangle$ contributions compared to the dominant ejections and sweeps. Furthermore, their profiles are close to symmetrical around the abscissa, leading to a negligible net contribution all over the profile. Unlike for the Reynolds stress, the opposite sign in w' between ejections and sweeps induce opposite signs in their $\langle Fk_q \rangle$ contributions ($\langle Fk_{IV} \rangle < 0$ while $\langle Fk_{II} \rangle > 0$). Consequently, the net DA vertical TKE flux is roughly equal to the residue between ejection and sweep TKE flux contributions while the net DA Reynolds stress is roughly equal to the cumulative ejection and sweep shear stress contributions. This difference shows similarities with Raupach *et al.* (1981) and Hurther *et al.* (2007) observations that TKE flux is linked to a residual difference between ejections and sweeps whereas the net TKE shear production relies on the cumulative shear contribution of ejections and sweeps.

As a result it is seen that the total DA TKE flux has a much lower absolute magnitude than both ejection and sweep contributions because their sum is small relative to their individual magnitudes. The minimum of the total DA TKE flux observed in the interfacial sublayer is seen to be associated with the negative vertical gradient of the sweep contribution being higher than the positive gradient of the ejection contribution. Outside the interfacial sublayer, the positive net DA TKE flux seems to follow the positive (i.e. ascendant) residual TKE flux between sweeps and ejections due to the stronger ejection contribution.

5.1.3. *Time fraction*

The DA time fractions associated with quadrants I and III are similar in shape and magnitude with a rather constant value of about 15 % outside the interfacial sublayer (see figure 7). Below z_c, their time fractions increase monotonically towards the bed with a maximum value of 25 % rather equally distributed over the four quadrants. Yue *et al.* (2007) found similar time fraction values within a corn field canopy. The profiles of time fractions associated with ejections and sweeps denote more pronounced differences in shape and magnitude. Outside the interfacial sublayer, the sweep time fraction is larger than the ejection time fraction while the DA shear stress and DA TKE flux from ejections are stronger than the respective sweep contributions. The contrary occurs within the interfacial sublayer. This reveals that the intensities of shear stress (ratio $\langle RS_q^* \rangle$ over $\langle T_q \rangle$) and TKE flux ($\langle Fk_q \rangle / \langle T_q \rangle$) events resulting from sweeps are larger than those resulting from ejections within the interfacial sublayer. Again, the contrary is true above the bed crest level z_c.

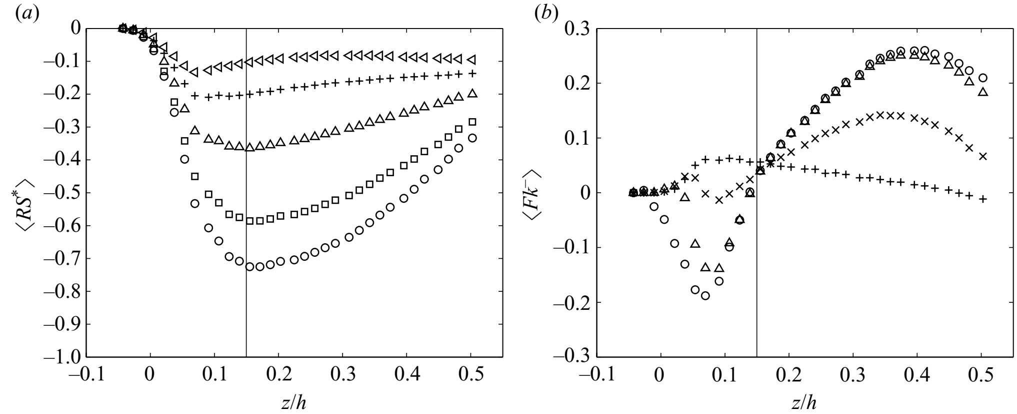

FIGURE 8. (*a*) Double averaged normalized Reynolds stress for events stronger than H with (○): $H = 0$, (□): $H = 2$, (△): $H = 4$, (+): $H = 6$ (◁): $H = 8$. (*b*) Normalized TKE flux for events weaker than H with (+): $H = 6$, (x): $H = 10$, (▷): $H = 20$, (○): Fk total. All quadrants considered.

In summary, the sweep events have a larger relative contribution compared to the other quadrants in DA Reynolds stress and DA TKE flux within the gravel-bed interfacial sublayer, and that their intensity is larger than the ejections in this flow region. Oppositely, ejection contribution and intensity is the largest above the interfacial sublayer, up to the intertial layer.

5.2. *Threshold level dependence of DA variables*

5.2.1. *Reynolds stress contribution*

Figure 8(*a*) shows similar profile shapes of the DA Reynolds stress contribution for various H. By definition, the DA Reynolds stress $\langle RS_q^* \rangle$ decreases with increasing H. We see that half the contribution occurs for events stronger than $H = 4$ and about 70 % is produced by events weaker than $H = 6$. This is in good agreement with results in Finnigan (2000) for a flow over a vegetated canopy.

5.2.2. *TKE flux contribution*

Figure 8(*b*) clearly reveals that events weaker than $H = 6$ and $H = 10$ do not reproduce the total DA TKE flux profile. Although all profiles intersect at $z/h = 0.18$, the shape and magnitude for events weaker than $H = 6$ is totally different. Indeed, a strong underestimation of $\langle Fk^- \rangle$ is seen above the bed crest level with a vertical gradient of opposite sign compared to the curves for $H > 6$. For events weaker than $H = 10$, the trends become locally similar to the total DA TKE flux, but still with magnitude discrepancies at all flow depths. Therefore, the DA TKE flux is seen to be driven by very intense shear events within and above the interfacial sublayer.

5.2.3. *Time fraction*

As expected, figure 9 shows that the time fraction of strong events decreases with increasing threshold level H. Events stronger than $H = 4$, which are responsible for 50 % of the DA Reynolds stress contribution (figure 8), occur during a DA time fraction of only 10 %. This result is in good agreement with the experimental results found in Finnigan (2000). Moreover, as previously seen in Nakagawa & Nezu (1977) for standard uniform rough-wall flows, the profiles indicate a substantial time fraction increase for all H level in the near bed region. Strong flow events are therefore more

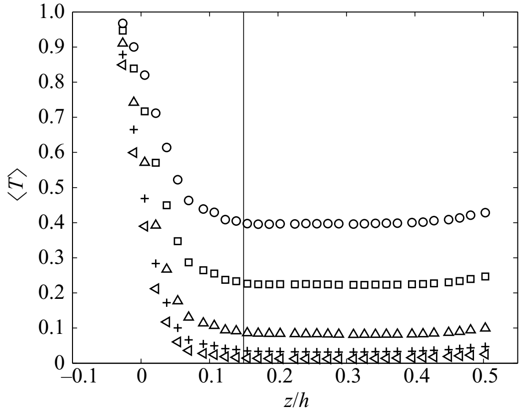

FIGURE 9. Double averaged duration fraction for Reynolds stress events stronger than H, with (○): $H = 1$, (□): $H = 2$, (△): $H = 4$, (+): $H = 6$ (◁): $H = 8$. All quadrants considered.

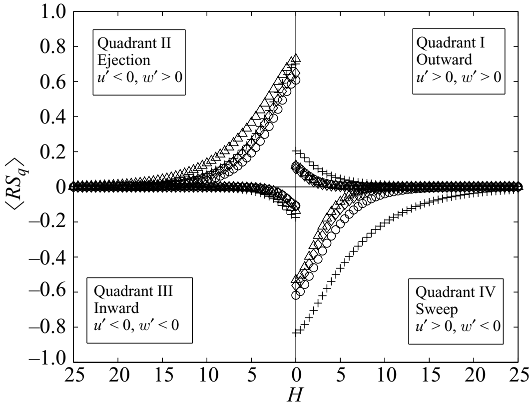

FIGURE 10. Double averaged quadrants at four elevations with (+): $z = z_c/2$, (○): $z = z_c$, (◇): $z = 2z_c$, (△): $z/h = 0.45$.

frequent within the gravel-bed interfacial sublayer than in the upper fraction of the roughness layer and the inertial layer.

In summary, 50 % of the DA Reynolds stress is produced by flow events of magnitude weaker than $H = 4$. However, these events produce a DA TKE flux profile totally different from the total DA TKE flux profile in terms of magnitude and shape.

5.3. *DA quadrants threshold distributions at different depths*

The DA Reynolds stress contribution by quadrant as a function of threshold at different depths is shown in figure 10. Their overall trends are very similar to those previously obtained in standard uniform rough-wall shear flows (Nakagawa & Nezu 1977; Raupach *et al.* 1981; Hurther *et al.* 2007; Yue *et al.* 2007). At any given H level, the sweep contribution decreases as z increases and the contrary is true for the ejection contribution. Quadrant I and III contributions remain small relative to ejection and sweep contributions, with negligible contributions for $H > 5$. Oppositely, ejections and sweeps remain active for $H > 5$, especially sweeps within the gravel-bed interfacial sublayer.

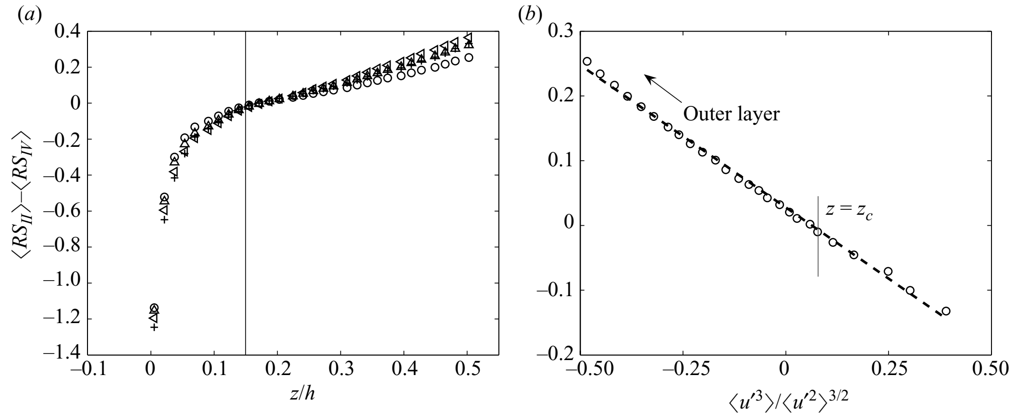

FIGURE 11. (*a*) Double averaged residual shear stress between sweeps and ejections for events stronger than H with (○): $H = 0$, (△): $H = 2$, (◁): $H = 4$, (+): $H = 6$. (*b*) Double averaged residual shear stress between sweeps and ejections for $H = 0$ plotted against the double averaged streamwise velocity skewness (straight line is the fitted linear relation).

Furthermore, at $z = z_c/2$ the four quadrant distributions are in very good agreement with those simulated by large eddy simulation (LES) in Yue *et al.* (2007) for a cornfield canopy. The very pronounced domination of sweeps at strong threshold levels is obviously a common feature between the vegetated canopy and the gravel-bed interfacial sublayer described herein.

5.4. *DA residual shear stress* $(\langle RS_{II}\rangle - \langle RS_{IV}\rangle)$

The notion of residual shear stress between ejection and sweep type events has first been introduced by Raupach *et al.* (1981) in standard uniform rough-wall shear boundary layers. Raupach *et al.* (1981) demonstrated empirically that third order turbulent velocity moments can be related linearly, leading to a simplified linear expression between the residual shear stress for $H = 0$ and the turbulent velocity skewness for the streamwise component:

$$RS_{II} - RS_{IV} = -0.37 M_{300} \tag{5.1}$$

with $M_{300} = \overline{u'^3}/\overline{u'^2}^{3/2}$.

Figure 11(*a*) shows the profile of DA shear stress residue for different threshold levels. For threshold level $H = 0$, the similarity with the profile of local residual shear stress in Raupach *et al.* (1981) is particularly good (please note that in Raupach *et al.* (1981) $\Delta S_0 = -(RS_{II} - RS_{IV})$). A linear relation between the DA residual shear stress for $H = 0$ and the DA turbulent velocity skewness for the streamwise component is also valid in our gravel-bed flow (figure 11*b*), but with a different coefficient:

$$\langle RS_{II}\rangle - \langle RS_{IV}\rangle = -0.44\langle\overline{u'^3}\rangle/\langle\overline{u'^2}\rangle^{3/2}. \tag{5.2}$$

This linear relation is found to be very robust, supporting the idea of a universal property. Furthermore, the equal DA shear stress contribution from sweeps and ejections is located at $z = z_c$ in our gravel-bed flow. In previous studies, this location rather corresponded to the delimitation between the inner and outer regions of the shear boundary layer but not to the top of the interfacial sublayer as here. Indeed, the roughness size in Raupach *et al.* (1981) and Hurther *et al.* (2007) was much smaller than the size of the inner region. Whether the bed crest level plays a dominant role

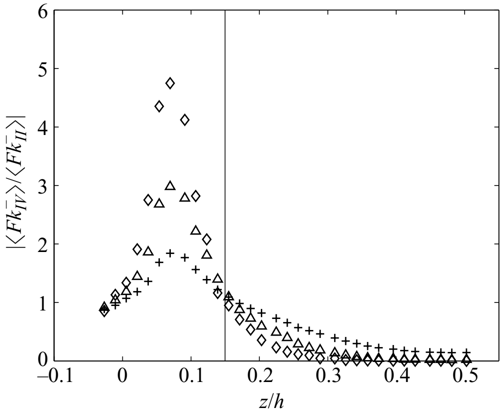

FIGURE 12. Double averaged TKE flux magnitude ratio between sweeps and ejections for events weaker than H with (+): $H = 6$, (△): $H = 10$, (◇): $H = 15$.

in (i) the coefficient values of the linear relation between the shear stress residue and third-order moments and (ii) the position of equal shear stress contribution between sweeps and ejections cannot be concluded from here but merits further investigation.

Moreover, in figure 11(*a*), the curve tendencies with H in the outer region denote a maximal shear stress residue for $H = 4$. The presence of a maximal residue at a threshold level around $H = 5$ has also been first found by Raupach *et al.* (1981) and later by Hurther *et al.* (2007). Within the interfacial sublayer, no minimum due to the excess of sweep contribution could be detected below $H = 6$. The negative residue is seen to increase with H in the interfacial sublayer, confirming the dominant contribution of intense sweeps due to roughness effects.

5.5. *DA TKE flux ratio between sweeps and ejections*

The role played by ejection and sweep events in the DA TKE flux is shown in figure 12 by the plot of the ratio between the DA TKE fluxes produced by sweeps ($\langle Fk^-_{IV}\rangle$) and ejections ($\langle Fk^-_{II}\rangle$) for events weaker than H (defined in (4.4)). It appears that within the interfacial sublayer, the sweep contribution is stronger by a factor of 2 at $H = 6$. Furthermore, this ratio increases by 50 % between $H = 6$ and $H = 10$, and even 2/3 between $H = 10$ and $H = 15$. This shows that very intense sweep events are responsible for the negative DA TKE flux in the interfacial sublayer. Outside the interfacial sublayer, ejections are seen to be the dominant contributors.

6. Bed zone specific characteristics of DA variables

The previous sections analysed the characteristics of the global DA quadrant threshold variables for Reynolds stress and TKE flux that have been spatially averaged over the entire measuring domain. This section aims at investigating bed zone specific characteristics of DA quadrant threshold variables based on the classification of velocity profiles presented in §§ 1 and 3. Whether the Reynolds stress and TKE flux dynamics produced by flow structures follow this bed zone specific organization or not is addressed below.

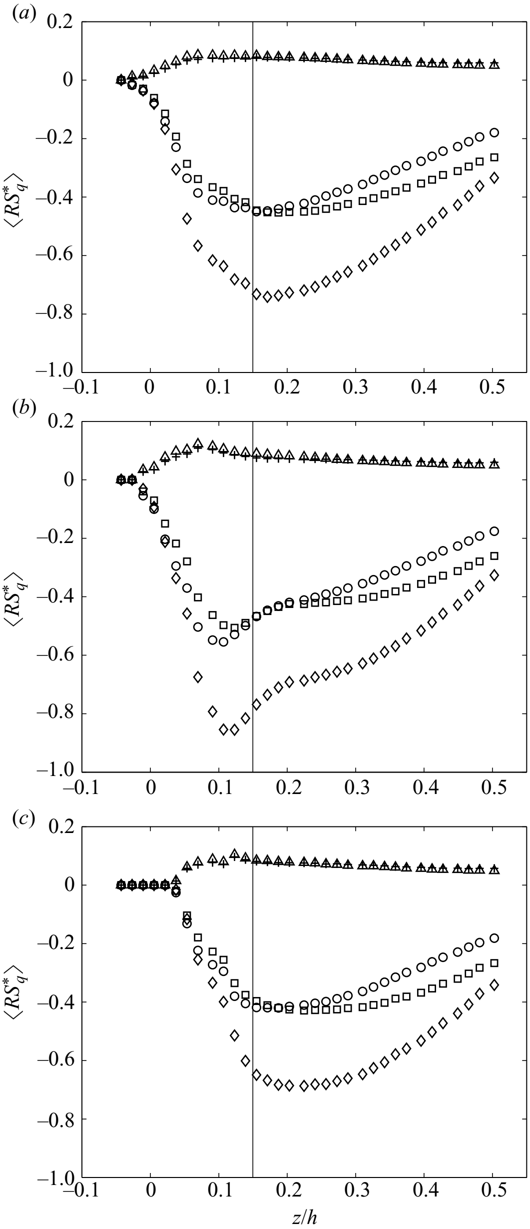

FIGURE 13. Per-class normalized Reynolds stress contribution from the four quadrants ($H = 0$) for log-class (*a*), S-shape-class (*b*) and accelerated-class (*c*) with (◇): total, (△): $q =$ I, (□): $q =$ II, (+): $q =$ III (○): $q =$ IV.

6.1. *Quadrant specific signatures of per-class averages*

6.1.1. *Reynolds stress contribution*

Figure 13 represents the three per-class Reynolds stress contributions for all quadrants along with the global DA Reynolds stress profile. It is seen that both log and accelerated classes have similar profile shapes, being in good agreement with the DA Reynolds stress profile. The S-shape profile deviates from the DA Reynolds

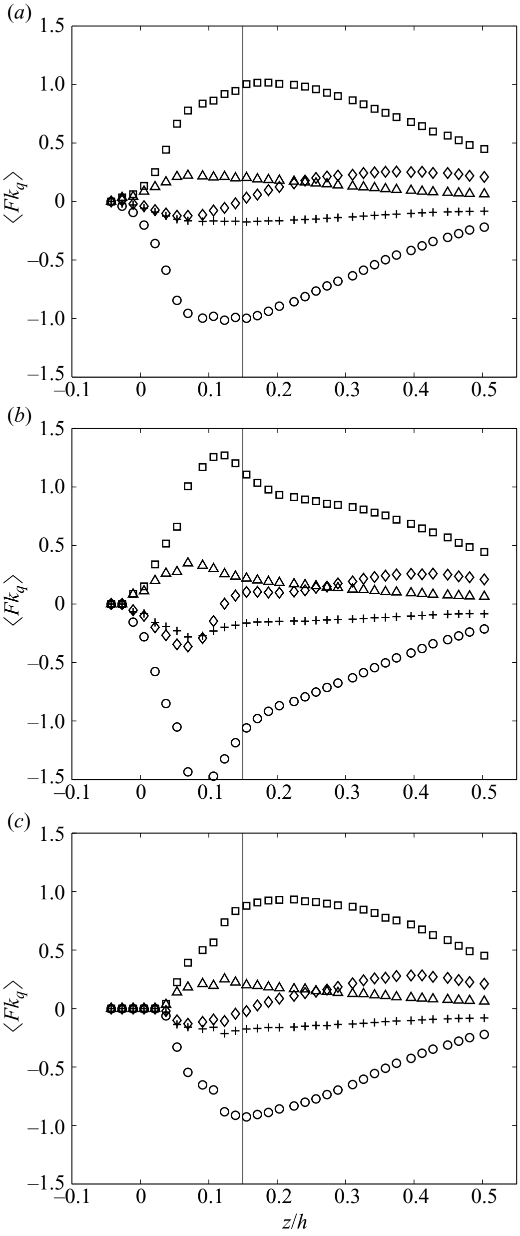

FIGURE 14. Per-class normalized TKE flux contribution from the four quadrants ($H = 0$). See figure 13 for legend.

stress profile in the interfacial sublayer with an excess of shear stress for both ejection and sweep events.

6.1.2. *TKE flux contribution*

The same behaviour is shown in figure 14 for the TKE flux contribution. The excess of $\langle Fk \rangle$ slightly below z_c is seen for all four quadrants in the per-class averaged S-shape profiles. However, when compared to the global DA $\langle Fk_q \rangle$, the $\langle Fk_{IV} \rangle$ increase in the interfacial sublayer of the S-shape-class (50 % increase) is larger than for the other quadrants (about 25 %). This leads to a significant increase of global DA TKE flux in the interfacial sublayer.

In summary, the excess of Reynolds stress in the interfacial sublayer for the per-class S-shape profile is due to a large increase of shear stress in both quadrants II and IV, while the excess of negative $\langle Fk \rangle$ in this S-shape class profile is induced by a large excess of sweep related TKE flux.

6.2. *Threshold level dependence of the per-class averages*

6.2.1. *Reynolds stress contribution*

The Reynolds stress contributions for different threshold levels (not shown here) for the three per-class-averaged profiles are similar to the global DA profile (shown in figure 8*a*). Moreover, the elevation of maximum shear stress value seems to shift towards the bed with increasing H in the S-shape-class-averaged profile, confirming the occurrence of very strong Reynolds stress events in the interfacial sublayer of the associated S-shape bed zones.

6.2.2. *TKE flux contribution*

The $\langle Fk \rangle$ contribution for different threshold level shown in figure 15 reveals the same tendency for the three classes as for the DA TKE flux: very intense events (between $H = 10$ and $H = 20$) strongly contribute to the TKE flux over the entire profiles. The importance of the intense events is particularly pronounced in the interfacial sublayer of the S-shape-class profile where events for $H > 20$ have a non-negligible contribution to the TKE flux.

6.3. *Per-class quadrant threshold distributions at different depths*

The per-class averaged quadrants in figure 16 are similar to the global DA quadrant graph (shown in figure 10) for elevations higher than $z_c/2$. At $z_c/2$, i.e. within the interfacial sublayer, the sweep excess is much more pronounced for the S-shape-class quadrant graph than for the log-class one. This excess is observed for all threshold levels H as for the measurements in a cornfield canopy flow by Yue *et al.* (2007) . It is however more pronounced for larger H levels. As a consequence, at $z_c/2$ the strong shear stress contribution of the sweep events from the S-shape-class tends to increase the global DA sweep related shear stress (figure 10) compared to the log-class sweep contribution.

7. LC3S's contribution to TKE flux across the gravel-bed roughness layer

The detection of coherent flow structures relies on the identification of spatially delimited flow regions containing turbulent velocity vectors in the same quadrant. Figure 2 reveals the occurrence of such macro-scale coherent flow structures of ejection and sweep types for a threshold value $H = 2$. The selected flow regions show coherent turbulent velocity fields over large fractions of the boundary layer height. They appear very similar in terms of size, occurrence and shape to the LC3S studied by Hurther *et al.* (2007) in a standard rough-wall channel flow. It was shown that LC3S are associated with zones of uniform streamwise momentum observed in the outer region due to the organization into macro-scale packets of hairpin vortices detached from the inner region (Adrian, Meinhart & Tomkins 2000; Ganapathisubramani, Longmire & Marusic 2003). The residual mean shear stress of LC3S was found to carry most of the mean TKE flux across the outer region for $0.25 < z/h < 0.75$. Moreover, the LC3S were seen to be disconnected from the wall region processes in these standard rough-wall shear flows.

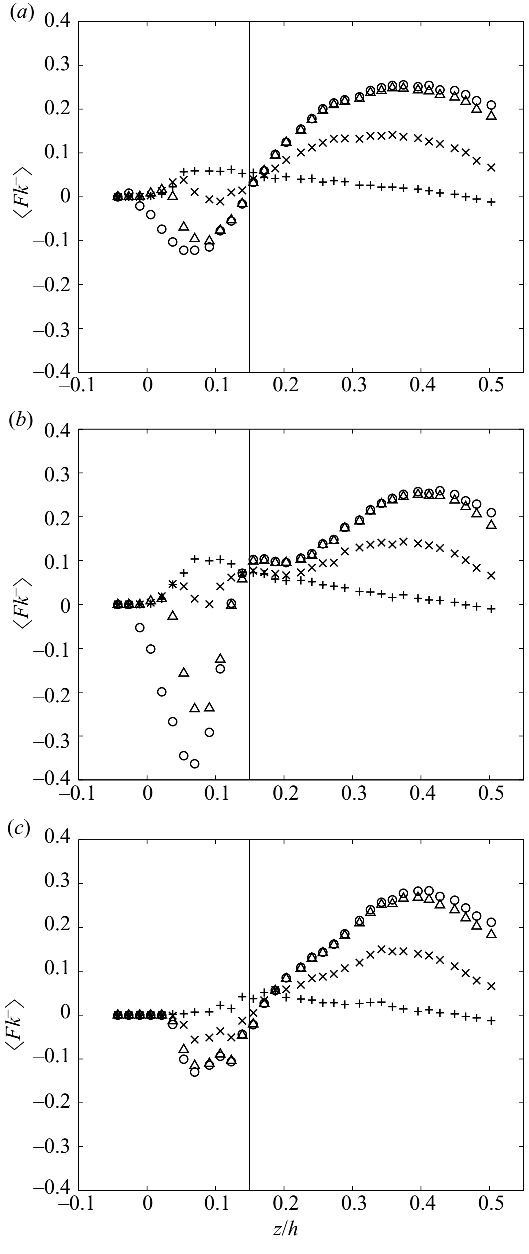

FIGURE 15. Per-class normalized TKE flux for events weaker than H for log-class (*a*), S-shape-class (*b*) and accelerated-class (*c*) with (+): H = 6, (x): H = 10, (▷): H = 20, (○): Fk total. All quadrants considered.

In order to determine the LC3S's contribution for the TKE flux, only the structures linking directly the roughness layer to the outer region have been selected. For this purpose, we introduce a third sampling condition in the selection of LC3S : each closed shear stress contours of LC3S must intersect both the lower limit (LL) and upper limit (UL) represented in figure 17. The limits are chosen to correspond to the zone 2 where the hairpin packets develop, as introduced by Adrian *et al.* (2000)

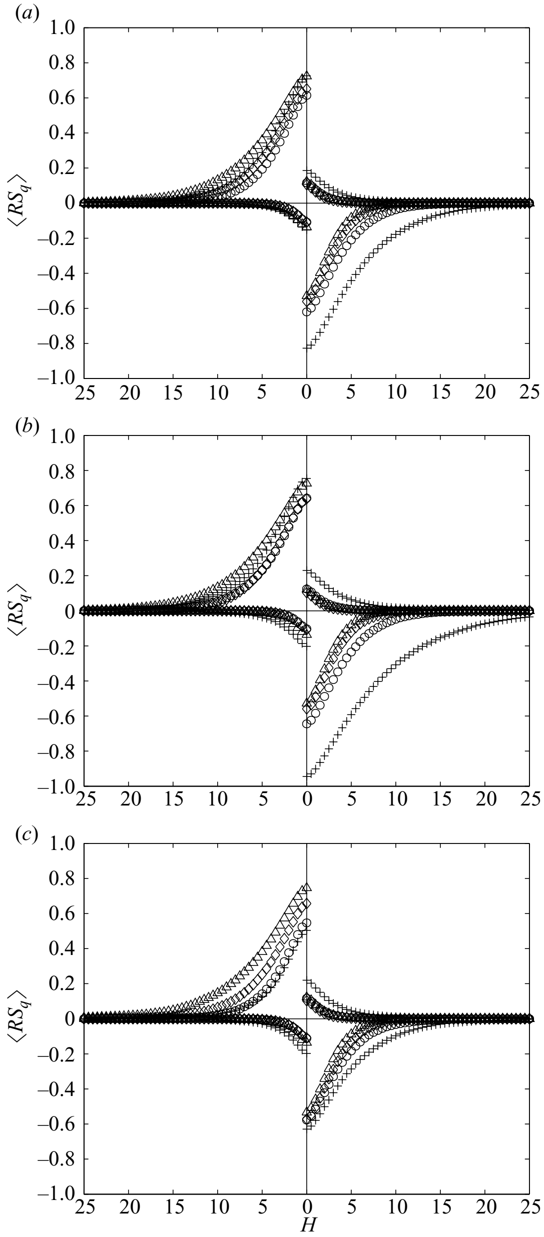

FIGURE 16. Per-class quadrants at four elevations for log-class (*a*), S-shape-class (*b*) and accelerated-class (*c*) with (+): $z = z_c/2$, (○): $z = z_c$, (◇): $z = 2z_c$, (△): $z/h = 0.45$.

and retrieved in Hurther *et al.* (2007). In the present gravel-bed flow conditions, the resulting LL is located at the top of the interfacial sublayer.

Figures 2 and 17 show that the selected LC3S are able to penetrate within the gravel-bed interfacial sublayer suggesting a direct link between the roughness layer and the outer region. Considering that LC3S are induced by an outer flow organization mechanism (Adrian *et al.* 2000; Hurther *et al.* 2007), this striking observation motivates us to calculate the importance of LC3S's contribution to DA TKE flux across the roughness layer.

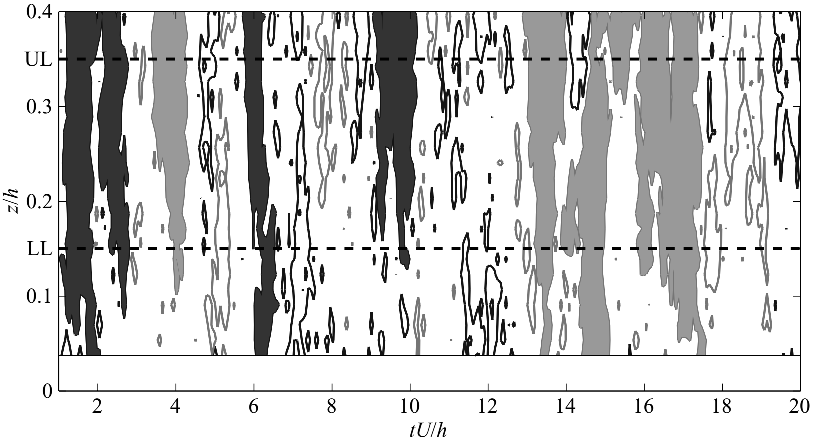

FIGURE 17. Time series of coherent structure detection with $H = 2$ at $x = 4.7$ m. Light grey = ejection structures and dark grey = sweep structures. Filled areas are LC3S. Dashed lines = lower (LL) and upper (UL) limits.

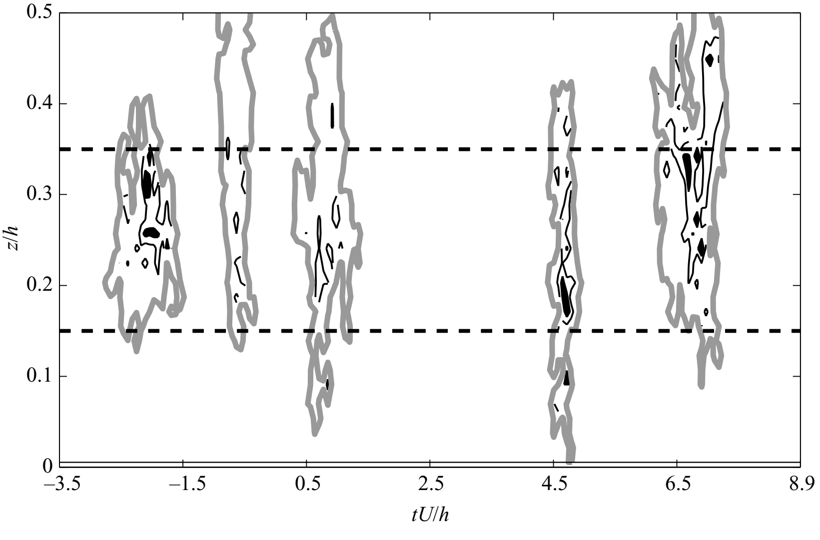

FIGURE 18. Time series of intense structures comprised within LC3S (for a S-shape-class profile) with grey thick lines: LC3S contours, black lines: $H = 6$ and filled areas: $H = 10$.

The DA LC3S variables are calculated as follows. In a first step, we select all sweep type LC3S (named S-LC3S in the sequel) and ejection type LC3S (E-LC3S) at each one of the 45 profiles. An example of this sampling technique is shown in figure 17 where the light and dark grey shades correspond to E-LC3S and S-LC3S, respectively. The DA TKE flux associated with E- and S-LC3S respectively are calculated : (i) by applying a time averaging of the selected LC3S (the dark or light shaded areas in figure 17) and (ii) using (3.1) for the spatial averaging. Because it was shown earlier in figure 8(*b*) that 75 % of the total TKE flux in the interfacial sublayer originates from flow structures (essentially sweeps) of level higher than $H = 10$, we calculate the DA TKE flux of LC3S for high threshold values in the same range (from $H = 6$ to $H = 10$). Figure 18 shows the contours of the selected structures within LC3S for

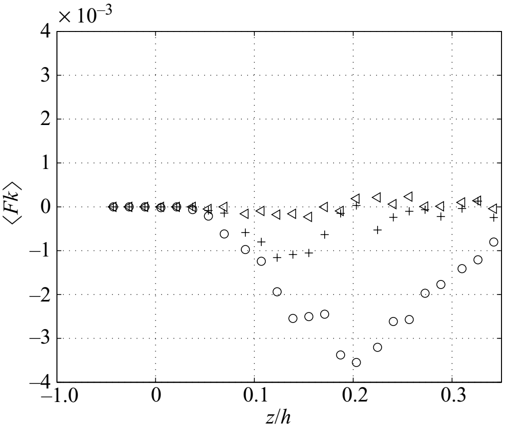

FIGURE 19. Contribution to TKE flux from intense events comprised within LC3S with (○): $H = 6$, (+): $H = 8$ and (◁): $H = 10$.

$H = 6$ and $H = 10$. The area of the selected structures appear to decrease rapidly with H. In figure 19, the corresponding profiles of TKE flux contributions are plotted for $H = 6$, 8 and 10. It is seen that compared to the total DA TKE flux (see figure 8), the contributions of LC3S for all three threshold levels are negligible. It can be deduced that LC3S do not contribute to the net TKE flux across the roughness layer although they can penetrate it intermittently.

The flow visualizations in figure 20 confirm qualitatively the previous results. At high threshold levels ($H = 22$) in the interfacial sublayer, mostly intense sweeps are active in both bed zones with obviously a much higher occurrence in gravel protuberance zones associated with the S-shape class.

8. Discussion and conclusion

The studied gravel-bed roughness layer is characterized by a strong spatial variability of all time-averaged flow quantities over a flow region reaching up to 40 % of the water depth starting at the bed. This variability is attributed to the spatial heterogeneity of the bed roughness structure appearing as a multi-scale roughness combination of bed zones with few emanating bed protuberances (or gravel clusters) acting as local flow obstacles, and zones of more homogenous roughness of densely packed gravel elements. Considering the complexity of this near-bed interfacial sublayer, we have applied a spatio-temporal averaging to the analysed flow quantities named DA. Three aspects have been addressed for the detailed examination of the shear stress and TKE flux structure across the gravel-bed roughness layer: (*a*) the DA shear stress (Reynolds and dispersive terms) and DA TKE flux (Reynolds and dispersive terms) in specific bed zones associated with three classes of velocity profiles as previously proposed in Hoover & Ackerman (2004) and Mignot *et al.* (2009); (*b*) the global and per class DA conditional statistics of shear stress and associated TKE flux and (*c*) the contribution of LC3S to the TKE flux across the roughness layer.

(*a*) In the interfacial sublayer, the DA Reynolds shear stress for the S-shape class exhibits a much stronger activity compared to the log and accelerated classes. As previously shown in Mignot *et al.* (2009), this is attributed to the detached mixing layer analogy of the flow characteristics in the S-shape class. The DA dispersive shear stress is dominant in the bed protuberance zones associated with the S-shape/accelerated

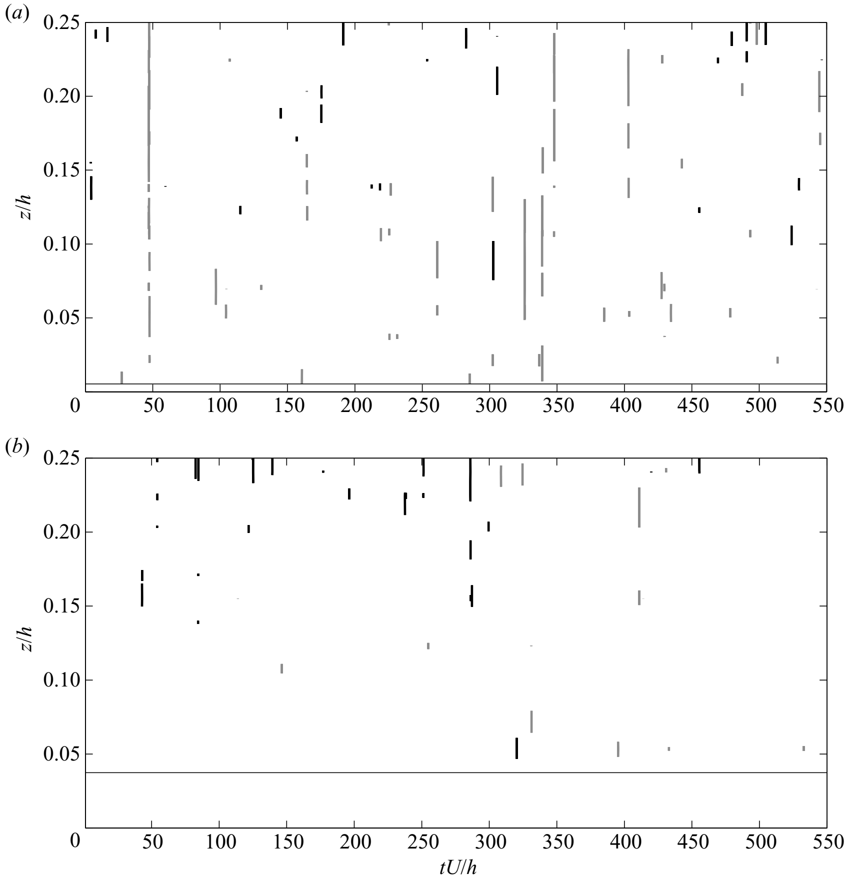

FIGURE 20. Time series of intense structures of ejection (black) and sweep (grey) with $H = 22$. (a) S-shape-class at $x = 4.4$ m, (b) log-class at $x = 4.7$ m

classes compared to the log class. In the later, the roughness structure is found to be more homogenous spatially due to the densely packed gravel elements and the absence of large-scale bed protuberances. The DA dispersive shear stress profile in the interfacial sublayer of the S-shape class, is in good agreement with the values measured by Pokrajac *et al.* (2008) for a d–k transition case in a standard rough-wall flow over square bars. Furthermore, we detect a lower DA Reynolds stress correlation coefficient all across the roughness layer for the S-shape/accelerated classes compared to the log-class. This is in good agreement with the recent measurements of Djenidi *et al.* (2008) in two k-type roughness flows. They attributed the decrease of DA Reynolds correlation between their two flows to the increase of streamwise separation distance between roughness elements. In our gravel bed flow, the streamwise distance between the bed protuberances for the S-shape/accelerated classes is also significantly higher (about $10k$) than the mean gravel separation distance (about k) in the bed zones of the log-class. These results suggest that even if the gravel roughness presents a complex random multi-scale roughness structure being very different from organized roughness of k and d-types, the protuberance bed zones act as k-type flow obstacles inducing a strong turbulent activity in their wake regions. These regions exhibit persistent S-shape velocity profiles, as shown in Mignot *et al.* (2009), in good agreement with the inflexional velocity profiles measured over groups of urban-like cubical obstacles (Coceal *et al.* 2006). Finally, as for the shear stress, the Reynolds and dispersive TKE flux are dominant for the S-shape class.

(*b*) Regarding the global DA conditional statistics, we find that above the interfacial sublayer delimited by the bed crest level z_c (at $z/h = 0.15$), the quadrant signatures are in good agreement with the results found in standard uniform rough-wall flows. In particular, the contribution of ejection events are dominant above z_c and ejections increasingly exceed the sweep contribution with distance from z_c and with threshold level H. Within the interfacial sublayer, i.e. below z_c, the DA contribution of sweeps in terms of Reynolds shear stress and TKE flux exceeds the ejection contribution. This excess in contribution increases with penetration into the interfacial sublayer and with threshold level H. In particular, we see that 75 % of the DA TKE flux is carried by very intense sweep events of relative intensity between $H = 10$ and $H = 20$. This sweep dominance across the interfacial sublayer causes the DA TKE flux to be oriented downwards. Literature results (Raupach *et al.* 1981; Nakagawa & Nezu 1977; Hurther *et al.* 2007) also show an excess of sweep contribution in the near-bed region of standard rough-wall flows. However, in our gravel-bed study, the position where sweeps start to exceed ejection contribution corresponds to the top of the interfacial sublayer at $z = z_c$, while this position is located far above the position of interfacial sublayer in standard rough-wall flows. Nevertheless, Yue *et al.* (2007) also found recently that this position corresponds to the top of the canopy in an atmospheric boundary layer over a corn field. Consequently, sweep events appear to be the dominant contributors to turbulent activity in all type of rough bed near-bed regions. However, the relative position (normalized by the flow depth or boundary layer thickness) at which their contribution becomes dominant seems to depend both on a roughness size parameter (such as z_c) and on a small-scale turbulent parameter (such as the Taylor micro-scale, see table 1) when the later is larger than the roughness size.

The results of the per-class DA conditional statistics put into evidence the effects of local bed protuberances on the quadrant signatures across the gravel-bed roughness layer. This can be seen from the quadrant results obtained for the S-shape-class corresponding to bed protuberance bed zones. In particular, inside the interfacial sublayer, the cumulative Reynolds stress linked to ejections and sweeps is about 40 % higher than for the log and accelerated classes. For the TKE flux of the S-shape-class, ejection and sweep events have the opposite sign and are respectively about 30 % and 50 % higher than for the log and accelerated classes. The contribution to the total TKE flux from inward and outward events is negligible within and above the interfacial sublayer for all classes. The total TKE flux associated with the S-shape-class is finally 300 % higher than in the log and accelerated classes within the interfacial sublayer. This drastic increase in S-shape-class to downward oriented TKE flux is associated with a larger negative vertical gradient of the sweep-related TKE flux profile in the interfacial sublayer compared to the lower positive vertical gradient for the ejection-related profile. The absolute difference in vertical gradients between sweep and ejection profiles is roughly four times smaller for the log and accelerated classes compared to the S-shape class. This confirms the dominant TKE flux contribution of sweeps in the bed protuberance zones associated with the S-shape-class. The zones downstream local bed protuberances appear to be crucial contributors to vertical TKE exchange.

(*c*) The visualization of coherent Reynolds stress events shows that LC3S, usually responsible for carrying most of the TKE across the outer flow region in standard uniform rough-wall channel flows (Hurther *et al.* 2007), are able to penetrate the interfacial sublayer intermittently. Nonetheless, their contribution to the total DA TKE flux is negligible. Indeed, 75 % of the total DA TKE flux are generated by coherent flow events (essentially sweeps in the interfacial sublayer) of level higher than $H = 10$. At this threshold level, LC3S become part of the hole events. Consequently, most of the very intense small-scale structures, which are active for the TKE flux, are not LC3S.

Unfortunately, our measurements do not allow a quantitative study of the vortex shedding process in the vicinity of the gravel bed due to the lack of spatial resolution with our ADVP system. In particular, transverse vorticity estimations are strongly affected by spatial averaging effects over the sample volume and by Doppler phase noise effects. Nevertheless, the averaged TKE budget terms presented in Mignot *et al.* (2009) strongly support the contribution of vortex shedding downstream the bed protuberances. The calculated local flow characteristics are in very good agreement with those obtained in the literature for detached mixing layers downstream backward facing steps. In a certain sense, the results found here go in that direction because as shown in figure 20, the scales of the dominating sweep-type events are of much smaller size than the large-scale coherent flow structures associated with the presence of hairpin packets (called LC3S in Hurther *et al.* 2007). It is possible that these small-scale very energetic turbulence structures are somehow a consequence of vortex shedding behind gravel clusters.

In conclusion, we showed that while Reynolds stress contribution is fairly well distributed between sweep and ejection events, with threshold values ranging from $H = 0$ to $H = 8$, the TKE flux across the roughness layer primarily results from the residual difference between ejection and sweep of very high magnitude ($H = 10$–20) and of small turbulent scale. These very energetic sweep events are dominantly produced in the bed zones located downstream the local gravel protuberances. In these protuberance wake regions, the velocity profiles are inflexional of S-shape type and the mean flow properties are of mixing layer flow type as shown in Mignot *et al.* (2009).

We are deeply indebted to Jean-Marc Barnoud, who renovated the LEGI flume, the ‘Ecole Nationale Supérieure d’Energie Eau et Environnement de Grenoble’ who provided the funding for this rehabilitation. We are also grateful to the European FP6 project ‘Hydralab III – Sands’ for their financial support. We are also thankful to the three anonymous reviewers for their helpful comments that improved the quality of this paper.

REFERENCES

Aberle, J. 2007 Measurements of armour layer roughness geometry function and porosity. *Acta Geophys.* **55** (1), 23–32.

Adrian, R. J., Meinhart, C. D. & Tomkins, C. D. 2000 Vortex organization in the outer region of the turbulent boundary layer. *J. Fluid Mech.* **422**, 1–54.

Antonia, R. A. & Atkinson, J. D. 1973 High-order moments of reynolds shear stress fluctuations in a turbulent boundary layer. *J. Fluid Mech.* **58** (3), 581–593.

Blanckaert, K. & de Vriend, H. J. 2004 Secondary flow in sharp open-channel bends. *J. Fluid Mech.* **498**, 353–380.

Blanckaert, K. & de Vriend, H. J. 2005 Turbulence structure in sharp open-channel bends. *J. Fluid Mech.* **536**, 27–48.

Castro, I. T. 2007 Rough-wall boundary layers: mean flow universality. *J. Fluid Mech.* **585**, 469–485.

Cheng, H. & Castro, I. T. 2002 Near wall flow over urban-like roughness. *Bound.-Layer Meteorol.* **104**, 229–259.

Christen, A., Van Gorsel, E. & Vogt, R. 2007 Coherent structures in urban roughness sublayer turbulence. *Intl J. Climatol.* **27**, 1955–1968.

Coceal, O., Thomas, T. G., Castro, I. P. & Belcher, S. E. 2006 Mean flow and turbulence statistics over groups of urban-like cubical obstacles. *Bound.-Layer Meteorol.* **121**, 491–519.

Djenidi, L., Antonia, R., Amielh, M. & Anselmet, F. 1994 Lda measurements in a turbulent boundary layer over a d-type rough wall. *Exp. Fluids* **16** (5), 323–329.

Djenidi, L., Antonia, R., Amielh, M. & Anselmet, F. 2008 A turbulent boundary layer over a two-dimensional rough wall. *Exp. Fluids* **44** (1), 37–47.

Finnigan, J. 2000 Turbulence in plant canopies. *Annu. Rev. Fluid Mech.* **32**, 519–571.

Franca, M. J. 2005 Flow dynamics over a gravel riverbed. In *Proceeding XXXI IAHR Congress*, Seoul, Korea.

Ganapathisubramani, B., Longmire, E. K. & Marusic, I. 2003 Characteristics of vortex packets in turbulent boundary layers. *J. Fluid Mech.* **478**, 35–46.

Grass, A. J. 1971 Structural features of turbulent flow over smooth and rough boundaries. *J. Fluid Mech.* **50**, 233–255.

Grass, A. J., Stuart, R. J. & Mansour-Tehrani, M. 1991 Vortical structures and coherent motion in turbulent flow over smooth and rough boundaries. *Phil. Trans. R. Soc. Lond.* A **336**, 35–65.

Hoover, T. M. & Ackerman, J. D. 2004 Near-bed hydrodynamic measurements above boulders in shallow torrential streams: implications for stream biota. *J. Environ. Engng Sci.* **3**, 365–378.

Hurther, D. & Lemmin, U. 2000 Shear stress statistics and wall similarity analysis in turbulent boundary layers using a high-resolution 3-d advp. *J. Ocean. Engng* **25** (4), 446–457.

Hurther, D. & Lemmin, U. 2001 A correction method for turbulence measurements with a three-dimensional acoustic doppler velocity profiler. *J. Atmos. Ocean. Technol.* **18** (3), 446–458.

Hurther, D. & Lemmin, U. 2003 Turbulent particle and momentum flux statistics in suspension flow. *Water Ressour. Res.* **39** (5), doi:10.1029/2001WR001113.

Hurther, D. & Lemmin, U. 2008 Improved turbulence profiling with field adapted acoustic doppler velocimeters using a bi-frequency doppler noise suppression method. *J. Atmos. Ocean. Technol.* **25** (2), 452–463.

Hurther, D., Lemmin, U. & Terray, E. A. 2007 Turbulent transport in the outer region of rough wall open-channel flows: the contribution of large coherent shear stress structures (lc3s). *J. Fluid Mech.* **574**, 465–493.

Jimenez, J. 2004 Turbulent flows over rough walls. *Annu. Rev. Fluid Mech.* **36**, 173–196.

Lemmin, U. & Rolland, T. 1997 Acoustic velocity profiler for laboratory and field studies. *J. Hydraul. Engnng* **123**, 1089–1098.

Liou, T. M., Chang, Y. & Hwang, D. W. 1990 Experimental and computational study of turbulent flows in a channel with two pairs of turbulence promoters in tandem. *J. Fluid Engng* **112**, 302–310.

Lopez, F. & Garcia, M. H. 2001 Mean flow and turbulence structure of open-channel flow through non-emergent vegetation. *J. Hydraul. Engng* **127** (5), 392–402.

Lu, S. S. & Willmarth, W. W. 1973 Measurements of the structure of the Reynolds stress in a turbulent boundary layer. *J. Fluid Mech.* **60**, 481–511.

Luchik, T. S. & Tiederman, W. G. 1987 Timescale and structure of ejections and bursts in turbulent channel flows. *J. Fluid Mech.* **174**, 529–552.

Mignot, E., Barthélemy, E. & Hurther, D. 2008 Turbulent kinetic energy budget in a gravel-bed channel flow. *Acta Geophys.* **56** (3), 601–613.

Mignot, E., Barthélemy, E. & Hurther, D. 2009 Double averaging analysis and local flow characterization of near bed turbulence in gravel-bed channel flows. *J. Fluid Mech.* **618**, 279–303.

Nakagawa, H. & Nezu, I. 1977 Prediction of the contribution to Reynolds stress from bursting events in open-channel flows. *J. Fluid Mech.* **80** (1), 99–128.

Nezu, I. & Nakagawa, H. 1993 Turbulence in open channel flows. IAHR Monograph. Balkema, Rotterdam.

Nikora, V., Goring, D., McEwan, I. & Griffiths, G. 2001 Spatially averaged open-channel flow over rough bed. *J. Hydraul. Engng* **127** (2), 123–133.

Nikora, V., McEwan, I., McLean, S., Coleman, S., Pokrajac, D. & Walters, R. 2007 Double-averaging concept for rough-bed open-channel and overland flows: theoretical background. *J. Hydraul. Engng* **133** (8), 873–883.

Perry, A. E., Schofield, W. H. & Joubert, P. N. 1969 Subelement form-drag parameterization in rough-bed flows. *J. Fluid Mech.* **37**, 383–413.

Pokrajac, D., Campbell, L. J., Nikora, V., Manes, C. & McEwan, I. 2007 Quadrant analysis of persistent spatial velocity perturbations over square-bar roughness. *Exp. Fluids* **42**, 413–423.

Pokrajac, D., McEwan, I. & Nikora, V. 2008 Spatially averaged turbulent stress and its partitioning. *Exp. Fluids* **45**, 73–83.

Raupach, M. R., Antonia, R. A. & Rajagopalan, S. 1981 Conditional statistics of Reynolds stress in rough wall and smooth wall turbulent boundary layers. *J. Fluid Mech.* **108**, 363–382.

Raupach, M. R., Antonia, R. A. & Rajagopalan, S. 1991 Rough-wall turbulent boundary layers. *Appl. Mech. Rev.* **44** (1), 1–25.

Robinson, S. K. 1991 Coherent motions in the turbulent boundary layer. *Annu. Rev. Fluid Mech.* **23**, 601–639.

Roth, M. 2000 Review of atmospheric turbulence over cities. *Quart. J. R. Meteorol. Soc.* **146**, 941–990.

Schlichting, H. 1936 Experimental investigation of surface roughness. In *Proc. Soc. Mech. Eng. NACA TM 823*, USA.

Song, T., Graf, W. H. & Lemmin, U. 1994 Uniform flow in open channels with movable gravel bed. *J. Hydraul. Res.* **32** (6), 861–876.

Sumer, B. M. & Deiggard, R. 1981 Particle motions near the bottom in turbulent flow in an open channel. Part 2. *J. Fluid Mech.* **109**, 311–337.

Yue, W., Meneveau, C., Parlange, M. B., Zhu, W., Van Hout, R. & Katz, J. 2007 A comparative quadrant analysis of turbulence in a plant canopy. *Water Ressour. Res.* **43** (5).